Sail aerodynamics: understanding pressure distributions on upwind sails

Viola, I.M., Flay, R.G.J.

Sail aerodynamics: Understanding pressure distributions on upwind sails

Experimental Thermal and Fluid Science 35 (2011) 1497–1504
doi:10.1016/j.expthermflusci.2011.06.009

Abstract

The pressure distributions on upwind sails is discussed and related to the flow field around the headsail and the mast/mainsail. Pressures measured on several horizontal sections of model-scale and full-scale sails are used to provide examples. On the leeward side of the sails, leading edge separation and turbulent reattachment occurs, sometimes followed by trailing edge separation. On the windward side, leading edge separation occurs on the mast/mainsail and, at low angles of attack, it can also occur on the headsail. Differences were found between the leading edge bubbles on the two sails. Pressure trends for different angles of attack are presented, and these can be explained in terms of standard aerodynamic theory, par- ticularly in terms of short and long leading edge separation bubble types. It was found that the pressure distributions measured on mainsails at full- and model-scale showed good agreement on both the wind- ward and leeward sides.

Nautical Nomenclature

Angle of attack (AoA)	The angle between the sail chord and the apparent wind direction.
Apparent and true wind	The '*apparent wind'* is the wind experienced by a sailing yacht andresults from the vector difference between the atmospheric boundary layer, namely the *'true wind'*, and the yacht velocity (Figure 1). The change in direction of the apparent wind velocity with the height is called the *'twist'*.
Apparent wind angle (AWA)	The supplementary angle between the yacht velocity and the apparent wind velocity.
Drive force	Aerodynamic force component in the direction of the yacht velocity.
Headsail and mainsail	Sail set forward and behind the mast, respectively, in a yacht with a single mast.
Slot Effect	The effect of the gap between the sails on their performance.
Upwash and downwash	Deflection of the streamlines beyond the top of a sail, and behind a sail, respectively, due to the generation of lift. Also used to describe the deflection of streamlines upstream and downstream of a sail, respectively, due to the generation of lift.
Upwind and downwind	Directions of the yacht with respect to the true wind. A yacht sails upwind and downwind when the angle between her velocity and the true wind is lower and higher than 90º respectively.
Windward and leeward	Side of the sail facing the wind and hidden from the wind, respectively.

Introduction

Numerical fluid dynamic methods are widely used to investigate sail aerodynamics. Potential flow codes are normally used to investigate sail aerodynamics in upwind conditions, when a mainsail and a headsail are used and the flow is mainly attached. Conversely, Reynolds Averaged Navier-Stokes techniques, and more recently Large Eddy Simulations, are used to investigate sail aerodynamics in downwind conditions, where the effect of trailing edge separation is not negligible. Although numerical simulations are very effective in investigating sail aerodynamics, they always need to be carefully validated with physical experiments.

Experimental measurements on sails are typically performed in wind tunnels. It is common practice to use flexible sails, which allow the sails to be trimmed. Aerodynamic forces are typically measured with a balance attached to the model. However, pressure measurements allow a more reliable validation of numerical simulations than force measurements. In fact, different pressure distributions can provide the same global aerodynamic forces. However, pressures are rarely measured. In fact, model-scale sails must be light and thin, which makes it difficult for pressure taps to be used. As far as is known to the present authors, pressure distributions on model-scale three-dimensional headsails and mainsails in upwind sailing conditions have never been published. Conversely, pressure distributions on full-scale sails were measured the first time between 1915 and 1921 (Warner and Ober, 1925) and much later by the present authors (Viola and Flay, 2010), and also by others, e.g. Puddu et al, 2006, and Gaves et al, 2008 .

In the present paper, pressure distributions on upwind sails were measured in a wind tunnel on horizontal sections of rigid pressure-tapped sails. Aerodynamic forces were measured with a 6-component balance placed below the model under the wind tunnel floor. The general pressure distributions on the headsail and the mainsail and the correlated flow fields are discussed. The pressure distributions are also compared with the recent full-scale tests performed by the present authors (Viola and Flay, 2010).

Method

The Yacht Research Unit (YRU) of the University of Auckland has developed an innovative pressure system capable of acquiring up to 512 channels at speeds up to 3,900 Hz on each channel. The transducers have a pressure range of ±450 Pa and a resolution of 9.25 mV/Pa. Although initially developed for laboratory use, it has been modified for use on the water. Additional details of the pressure system are provided in Viola and Flay (2010). The system was used to measure the pressures on model-scale rigid pressure-tapped sails, which were designed for the America's Cup class 'AC33'. A $1/15^{th}$-scale mainsail and headsail were built as fibreglass sandwich structures. The core was made of a 2 mm thick polypropylene plastic sheet, which had 3 mm wide core flutes. Pressures were carried along the sail in the core-flutes to the sail foot. Pressure tubes carried the pressure from the sail foot to the transducers, which were placed in the cockpit. The sails were perforated along 5 horizontal sections. On the 5 mainsail sections, 9, 11, 13 and 14 holes were used on the top to the bottom sections, respectively. On the 4 headsail sections, 7, 8, 11 and 15 holes were used on the top to the bottom sections, respectively. To measure the leeward side of the sail,

tape was used to close the holes on the windward side, and vice versa. In order to correctly model the leading edge flow field, the sails were chamfered at about 20° on the windward side to produce a sharp leading edge. Additional details of the sail construction can be found in Fluck et al, (2010).

The sails were fixed onto a model-scale yacht with a rigid mast, and were tested in the YRU Wind Tunnel (Figure 2). The wind tunnel is an open jet with a test section 7 m wide and 3.5 m high.

Four different mainsail and headsail trims, four AWAs (16°, 20°, 24° and 28°), several heel angles (from 0° to 20°), and several twists of the onset flow were tested. The results presented and discussed in the paper are restricted to those measured in upright sailing conditions and with no twist in the onset flow.

The reference static pressure p_∞ was provided by the static tap of a Pitot-static tube, which was located approximately at the same height as the top of the mast and 6 h upstream of the model (where h = 2.3 m is the model height). The difference between the total pressure tap and the static tap of the same Pitot-static tube was used to measure the reference dynamic pressure q_∞ = 32.5 Pa. The Reynolds number Re based on the average chord length c = 0.49 m was $Re = 2.3 \cdot 10^5$. The pressure measurement accuracy was estimated to be about ±0.5 Pa.

The same pressure system was used to measure the pressure distributions on full-scale sails. Pressures from 30 and 33 pressure taps on the mainsail and headsail, respectively, of a Sparkman & Stephens 24-foot yacht (SS24) were measured. Several sail trims and apparent wind angles were tested. The reference static pressure p_∞ was measured inside the yacht cabin. The dynamic pressure q_∞ was measured with Pitot-static tubes fixed onto a pole attached to the stern of the yacht. More details can be found in (Viola and Flay, 2010). Subsequent analysis showed that the dynamic pressure measured at this location was about 20% higher than the estimated far-field dynamic pressure due to the influence of the yacht and sails on the pressure measuring system. In the present paper, the corrected dynamic pressure has been used. The full-scale Re based on the mean chord (1.5 m) and the mean apparent wind velocity (6 m/s) was $Re = 6.1 \cdot 10^5$. Figure 3 shows a schematic drawing of the AC33 and the SS24 sailplans.

Both in the wind-tunnel tests and in the full-scale test, the pressure distributions showed the same qualitative trends with the AWA and the trim variations. The measured pressure trends can be explained in terms of conventional thin airfoil theory and the aerodynamic properties of separation bubbles. In the following, the measured pressure distributions on the sail sections are related to the angle of attack (AoA), which resulted from the sail trims and the AWAs (see Figure 1).

Pressure Distributions on the Headsail

Ideal AoA

The maximum drive force was achieved when the headsail was trimmed at, or slightly higher than, the *'ideal'* AoA, i.e. when the local flow is tangent to the sail at the leading edge (LE). The

stagnation point is then located at the LE, where the pressure coefficient, defined as $Cp = (p - p_\infty)/q_\infty$, is $Cp = 1$.

Figure 4 shows schematic diagrams of the anticipated streamlines around horizontal headsail sections trimmed at different AoAs. *Cps* plotted against the corresponding non-dimensional chords x/c are also shown. In particular, Figure 4B shows the streamlines around the headsail section trimmed at the ideal AoA.

On cambered sails, at the ideal AoA, an attached boundary layer grows from the LE on both sides of the sail. The sail curvature leads to suction and pressure peaks on the leeward and windward sides respectively, related to the position of maximum camber. At the trailing edge (TE), *Cp* is about zero or is slightly negative.

LE Separation Bubble

At AoAs higher than the ideal AoA, on the leeward side, the flow separates due to the sharp LE. Laminar to turbulent transition occurs on the separated shear layer and reattachment occurs. The resulting closed streamline flow pattern is called a *'LE separation bubble'*.

There are two types of LE separation bubbles: short bubbles, which typically occur on rounded-nose conventional airfoils, and long bubbles, which typically occur on thin airfoils. The first bubble type affects the performance of airfoils and it is of particular interest in aeronautical applications. Laminar to turbulent transition occurs in the downstreammost part of the bubble, and the reverse flow velocity inside the bubble is typically less than 20% of the free-stream velocity (Gault, 1957). Figure 5 shows a schematic diagram, which was drawn by Alam and Sandham (2000), of the short LE bubble structure described by Horton (1968).

The second LE bubble type became of interest in the 1950s, when high-speed aircraft adopted thin airfoils to decrease the effects of compressibility. Research on long bubbles also increased with the development of turbo-machinery, where thin blades are used, and with the growth of low-Reynolds-number aviation. The major characteristic of long LE bubbles is the generation of a large recirculation region with high backflow velocity. With long bubbles, separation occurs at the sharp LE. Laminar to turbulent transition occurs at the upstream end of the bubble. An investigation of laminar separation bubbles on flat plates performed at $Re = 2.13 \cdot 10^5$ (Crompton and Barret, 2000) shows that at least 95% of the shear layer is turbulent. Consequently, reattached flow is more energetic from the long bubble type than from the short bubble type, and backflow in the recirculation region is significantly faster. The centrifugal force that curves the flow inside the bubble is due to a high suction inside the recirculation region. The backflow that decelerates near the LE can itself separate due to the high positive pressure gradient, forming a secondary separation bubble. Figure 6 shows a schematic diagram of the long LE bubble type drawn by Crompton and Barret (2000).

Leeward Pressure Distribution on a Flat Plate

The stagnation point is theoretically exactly at the LE only at the ideal AoA. Indeed, practically, the stagnation point is at the LE for a wide range of AoAs around the ideal AoA. For instance, on a flat

plate, the ideal AoA occurs when the plate is aligned with the far-field wind direction (AoA=0°). However, Crompton and Barret (2000) found that the stagnation point was at the LE for $-20° < AoA < 20°$. They explained this finding by stating that: 'Although the leading edge appears to be sharp, it clearly must have thickness and be somewhat rounded'.

They also found that the suction peak, which has $Cp \approx -1$ and is correlated with the recirculation flow, occurs at around 30% of the bubble length. Downstream of the suction peak, the pressure increases asymptotically reaching $Cp \approx -0.1$ at the TE. Reattachment occurs downstream of the maximum pressure gradient, when $Cp \approx -0.3$. Increasing the AoA causes the reattachment point to move further downstream, and the maximum positive pressure gradient decreases, leading to a smoother *Cp* versus x/c curve.

AOAs > ideal AoA

At AoAs higher than the ideal AoA, the stagnation point is practically at the LE for all conditions of interest and, hence, $Cp \approx 1$ at the LE. The LE separation bubble occurs on the leeward side of the headsail. The pressure shows a minimum near the LE which is correlated with the suction inside the bubble, followed by a positive pressure gradient correlated with the reattachment point. Further downstream, a curvature-related suction peak occurs. Therefore, two suction peaks occur: the LE suction peak near the LE, and the curvature-related suction peak near maximum sail camber (see Figure 4C).

Too much sail curvature can lead to TE separation. In these circumstances, the mean stream velocity and the velocity gradients in the separated region are small and, hence, the pressure gradients downstream of the separation are small. Where separation occurs, the pressure recovery is interrupted, and the pressure remains almost constant at the so-called *'base pressure'* up to the TE.

As the AoA is increased, the LE bubble enlarges and the positive pressure gradient related to the reattachment decreases. The TE separation point moves upstream and, consequently, the curvature-related suction peak decreases. At very high AoAs, the reduction of the positive pressure gradient and of the curvature-related suction peak leads to a monotonic pressure recovery from the LE suction peak to the base pressure (Figure 4D).

AoA < ideal AoA

On flexible headsails, when the AoA is lower than the ideal AoA, the LE collapses. Conversely, on rigid sails, the sail shape does not change. In this latter case, decreasing the AoA causes a LE bubble to occur on the windward side of the sail, and the camber-related suction and pressure peaks on the leeward and windward sides respectively to decrease (Figure 4A).

LE Pressures on the Headsail

In viscous flow, the pressure distribution on the sail section is continuous. However, the pressure gradients at the LE can be extremely high. At the stagnation point, $Cp = 1$ and, as mentioned above, the stagnation point is usually at the LE.

At AoAs higher than the ideal AoA, on the windward side downstream of the stagnation point, *Cp* decreases at high rate. The closer the AoA to the ideal AoA, the more negative the gradient of *Cp* results. For instance, on the windward side of a flat plate, the pressure decreases monotonically up to the TE. At $\mathrm{AoA} = 1°$, *Cp* drops from $Cp = 1$ to $Cp \approx 0.2$ in the first 3% of the chord length, then it decreases at low rate until the TE where $Cp \approx -0.2$. At $\mathrm{AoA} = 5°$, *Cp* drops from $Cp = 1$ to only $Cp \approx 0.65$ in the first 3% (Crompton and Barret, 2000).

On the leeward side, the LE bubble occurs. The LE suction peak can be very close to the LE. The closer the AoA to the ideal AoA, the smaller the LE bubble, and the nearer to the LE the suction peak occurs.

As a consequence, at AoAs above the ideal AoA, the *Cp* is almost discontinuous at the LE, being between 0 and 1 on the windward side, and being lower than -4 on the leeward side.

In the present paper, the distances of the closest pressure taps from the LE and the TE (located at roughly 3% and 98% of the chord, respectively) do not allow the LE and the TE pressures to be measured on either side.

As mentioned earlier, the maximum *Cp* is assumed to be nearly equal to 1, but this can only be the case in two-dimensional flow. However, a cross-flow component can occur along a three-dimensional sail span. However, there must be one point on the sail where all the flow components are equal to zero and thus $Cp = 1$, but it does not have to occur on the LE of all the sail sections, so the maximum *Cp* on real three-dimensional sails could be 1 or slightly less than 1.

TE Pressures on the Headsail

At the TE of the headsail, the *Cp* is typically negative. It should be reiterated that, in inviscid flow, at the TE, $Cp = 1$ for thick airfoils while $Cp = 0$ for infinitely thin profiles. Negative *Cps* are related to separated flow.

At high AoAs, when TE separation occurs on the leeward side of the sail, pressure recovery is interrupted by the separation process. Therefore, the higher the AoA, the lower the TE pressure. If TE separation does not occur, the *Cp* at the TE is typically in the range $0 < Cp < -0.5$. For instance, Figure 7 shows *Cp* measured on the mid-height section of the model-scale headsail, at 4 different AWAs: 16°, 20°, 24° and 28°.

In Figure 7, the pressure distribution at AWA=20° corresponds to the ideal AoA, and to the flow field shown in Figure 4B. Similarly, the pressure distributions at 16°, 24° and 28° can be related to the flow field shown in Figures 4A, 4C and 4D respectively.

Windward Pressure Distributions on the Headsail

Figure 8 shows the windward *Cp* measured on the mid-height section of the model-scale headsail, for 4 different headsail trims and two AWAs. The ideal AoA is achieved by trim 'J2' at AWA=16°. The AoA increases when the headsail is tightened (from 'J4' to 'J1') and also when the AWA is increased (from 16° to 28°).

At AoAs greater than the ideal AoA, the stagnation point is on the windward side and the boundary layer is attached up to the TE. *Cp* is almost equal to 1 at the LE, and then decreases suddenly to lower values. Downstream, the sail curvature causes the *Cp* to increase again. Finally, near the TE, *Cp* drops down to negative values in order to match the *Cp* on the leeward side. Therefore, *Cp* shows a LE suction peak and a curvature related pressure peak.

Increasing the AoA causes the suction peak to decrease, while the curvature-related pressure peak increases. The higher the AoA, the further upstream the pressure peak occurs (e.g. see the curve for J1-16°). At high AoAs, the LE suction peak becomes negligible and the pressure decreases monotonically up to the TE (e.g. see the curve for J1-28°, where AoA = 28° and the trim is tight).

On rigid sails, the sail shape does not change when the AoA is lower than the ideal AoA. In these circumstances, the stagnation point is on the leeward side and the LE separation bubble occurs on the windward side. Near the LE, *Cp* is almost 1 on the leeward side, while it is lower than 1 on the windward side where, downstream, *Cp* decreases further due to the leading edge bubble. The windward suction peak is smoother than the suction peak that occurs on the leeward side at AoA larger than the ideal AoA. In fact, the LE bubble is thicker due to the concave shape of the sail and thus, it has lower backflow velocity. Downstream, *Cp* increases both due to reattachment and to sail curvature. The lower the AoA, the further downstream the reattachment occurs and, thus, the further downstream the positive pressure peak occurs (e.g. compare J3-16° and J4-16°).

Effect of the Mainsail

The lift generated by the mainsail has 2 consequences on the headsail pressure distribution. Firstly, it leads to an AoA increase for the headsail (upwash). In fact, when either the mainsail or the headsail is trimmed in, the measured pressure distribution trend on the headsail is similar. Secondly, the headsail TE pressure decreases due to the *'slot effect'* (Gentry, 1971), because the TE is in the mainsail suction region. Therefore, if TE separation does not occur, increasing the AWA or trimming in the mainsail, causes a lower pressure on the leeward side of the mainsail, which leads to a lower headsail TE pressure, and thus to more suction along its entire leeward side.

Pressure Distribution on the Mainsail

Pressure Distribution on the Leeward Side of Mast/Mainsail

When sailing upwind, the optimum mainsail trim varies significantly with the AWA and the full-scale dynamic pressure. Therefore, all the pressure distributions described in the following can be related to realistic trims.

The mast in front of the mainsail affects the flow on the rear part of the mainsail. The stagnation point is located on the mast and its position depends on the AWA and the mainsail trim. Moreover, its position depends also on the headsail trim, due to the downwash effect on the mainsail. In fact, when the mainsail is trimmed in or the headsail is eased, similar pressure trends occur on the mainsail.

On the leeward side, the flow accelerates around the mast curvature and a suction peak occurs. The high curvature of the mast causes the laminar boundary layer to separate. The laminar shear layer becomes turbulent and reattaches onto the mainsail surface. A low recirculation flow velocity and a low pressure gradient across the bubble are expected. In fact, the backflow is slowed down by the step made by the backward face of the mast. In the present paper pressures on the mast are not measured. However, Wilkinson (1984) measured pressures on a 2D mast/mainsail section. The headsail was not modelled in his experimental setup. The pressure distribution measured by Wilkinson is presented in Figure 9, where the roman numerals identify 9 topological regions. Wilkinson found that the pressure recovery is interrupted at the separation point. The pressure remains constant up to the laminar to turbulent transition in the rear part of the bubble. Downstream of the reattachment point, the pressure decreases again due to the sail curvature. In the present paper, the first pressure tap on the mainsail is located at around 3% of the chord length, where the pressure is already recovering following the laminar to turbulent transition. The pressure distributions measured in the present paper are qualitatively in agreement with Wilkinson's *Cp* trends shown in Figure 9.

Figure 10 shows *Cps* measured on the mid-height section of the model-scale mainsail, for 3 trims and 2 AWAs. The resulting AoA increases when the mainsail is tightened (from trim 'M4' to 'M1') and the AWA is increased (from 16° to 28°).

At low AoAs (M4-16°), the LE bubble is short and the pressure recovery is high. Positive values up to $Cp = 0.5$ were measured at the first leeward pressure tap. Downstream, suction due to the mainsail curvature occurs, which is significantly lower than the curvature-related suction occurring on the headsail. In fact, the curvature of the mainsail is lower than the curvature of the headsail. This moderate curvature makes TE separation less likely to occur.

Increasing the AoA (M1-16° and M1-28°), causes the LE suction peak to increase. The LE bubble enlarges and the increasingly negative maximum pressures occur further downstream. The curvature-related suction increases with increase in the AoA.

At very high AoAs (not shown in Figure 10), a monotonic pressure increase occurs. Increasing the AoA causes the monotonic pressure increase to occur earlier at the lowest mainsail sections where the sail is flatter, and at the highest sections where the curvature-related suction is smoothed due to

the TE separation, than at the mid-section. In fact, TE separation is more likely to occur on the highest sections of the mainsail that are above the top of the headsail, which therefore experience less downwash than the other sections.

As mentioned above, general agreement was found between the present measured pressure distributions and the pressure distributions measured by Wilkinson (1984). However, in the present paper, TE separation occurred at only very high AoAs, when the *Cp* showed a monotonic increase. Conversely, Wilkinson described a *Cp* trend where there were 2 suction peaks and a pressure plateau at the TE. An analysis of the schematic diagrams in Figure 4 shows that in the measurements performed by him, TE separation occurred at lower AoAs than in the present paper. It is expected that this is due to the fact that Wilkinson performed two-dimensional experiments, while in the present paper a finite-span three-dimensional mainsail was tested, which led to higher pressures on the leeward side of the sail (due to span-wise flows), and thus to TE separation at higher AoAs.

LE and TE Pressures on the Mast/Mainsail

On mast/mainsail sections, the stagnation point is on the mast. The cross-flow velocity along the mast is expected to be negligible and hence, *Cp* is expected to be exactly equal to 1.

The TE pressure is typically closer to zero on the mainsail than on the headsail. In particular, on the mainsail, *Cp* is almost 0 at the TE of the bottom sections, and decreases to slightly negative values towards the highest sections.

Windward Pressure Distribution on the Mast/Mainsail

On the windward side, downstream of the stagnation point on the mast, an attached boundary layer develops. The mast curvature causes the flow to accelerate and a suction peak occurs (Figure 9). The mast curvature leads to separation. Laminar to turbulent transition occurs in the separated shear layer, which helps the shear layer to reattach. Reattachment on the windward side can occur further downstream along the chord than reattachment on the leeward side of the sail. The recirculation flow has low mean velocity, which leads to a constant pressure along most of the bubble length. The *Cp* increases due to the reattachment. Downstream of reattachment, the pressure can increase even further due to the sail curvature, before decreasing at low rate to match the TE pressure.

At low AoAs, the windward LE bubble can extend to more than 3/4 of the chord length. On the bottom sections, the low sail curvature causes the reattachment to occur earlier than on the mid-sections, where the curvature is higher.

The LE bubble becomes shorter when the AoA is increased. Both the stagnation point and the separation point on the mast move downstream, while reattachment occurs closer to the LE on the mainsail. The pressure plateau is at a higher pressure, and the positive pressure gradient increases. At high AoAs, the pressure decreases monotonically from the LE to the TE.

Full-scale & Model-scale pressure distributions

No significant differences between the measured full-scale and the model-scale pressure trends were found. The pressure variations showed consistent trends but it was not possible to estimate the measurement accuracy.

A range of sail trims were tested in full scale as for the model-scale tests,. Figure 11 shows the *Cps* for the two full-scale ('FS') trims and the two model-scale ('MS') trims which led to the smallest positive and negative pressure difference between the windward and leeward sides of the sail at the LE. Hence the results presented herewith were selected from the results obtained on that basis, In particular, $Cp_{windward} - Cp_{leeward} > 0$ for the trims 'M1' and $Cp_{windward} - Cp_{leeward} < 0$ for the trims 'M2'. The FS and MS trims M1 are tighter than the FS and MS trims M2, respectively.

Figure 11 shows that the full-scale and model-scale *Cp* trends are in good agreement.

This was despite the fact that when $Cp_{windward} - Cp_{leeward} < 0$, the shape of the flexible sail tested in full-scale changed, while the rigid model-scale sail did not, and so such good agreement in the results is perhaps somewhat surprising.

Conclusions

The present paper aims to describe the general pressure distributions on upwind sails using conventional aerodynamic theory. The present results can be used to verify the capability of numerical simulations of modelling the pressure trends on upwind sails.

Pressure distributions were measured on a model-scale headsail and mainsail. The measured pressure distributions are discussed and related to the flow field for different angles of attack. Different pressure trends correlated with the leading edge bubbles on the headsail and mainsail have been presented. The observed results are in good agreement with the sparse literature on this subject.

The pressure distributions can be explained in terms of conventional aerodynamic theory for thin aerofoils. The flow field around the headsail and the mast/mainsail are significantly different due to the presence of the mast and thus their different leading edge shapes. While the headsail has a sharp leading edge, the mast/mainsail has a rounded leading edge. However, at angles of attack lower than the ideal angle of attack, a leading edge bubble occurs on both the headsail, due to the sharp leading edge, and on the mast/mainsail, due to the high curvature of the mast. The two leading edge bubbles have different characteristics, and so do the related pressure distributions.

The upwash on the headsail due to the mainsail, and the downwash on the mainsail due to the headsail, lead to lower pressures on the leeward side of the headsail than on the mainsail. The low pressure and the high curvature of the headsail can lead to trailing edge separation on any section of the headsail. Conversely, trailing edge separation can only occur at the highest sections of the mainsail, where the downwash due to the headsail is lower.

On the windward side of the two sails, the pressure coefficient is generally between 0 and +1 on most of the chord length. As an exception, on the mainsail at low angles of attack where the flow is

separated on both sides, the windward pressures can be significantly negative and the leeward pressures can be significantly positive.

References

Alam, M., Sandham N.D., 2000. Direct Numerical Simulation of 'Short' Laminar Separation Bubbles with Turbulent Reattachment. *J. Fluid Mech.*, 410, 1–28.

Crompton, M.J., Barret, R.V., 2000. Investigation of the Separation Bubble Formed Behind the Sharp Leading Edge of a Flat Plate at Incidence. *Proc. Inst. of Mech. Eng., Part G: J. of Aerospace Eng.*, 214 (**3**), 157-176.

Fluck, M., Gerhardt, F.C., Pilate. J., Flay, R.G.J., 2010. A Comparison of Potential Flow Based and Measured Pressure Distributions Over Upwind Sails, *J. of Aircraft*, 47 (**6**), 2174-2177.

Gault, D.E., 1957. An Investigation at Low Speed of the Flow Over a Simulated Flat Plate at Small Angles of Attacks Using Pitot Static and Hot Wire Probes, *NACA* TN-3876.

Gentry, A., 1971. The Aerodynamics of Sail Interaction, *Proc. 3rd AIAA Symp. on the Aero/Hydronautics of Sailing*, Nov. 20th, Redondo Beach, CA.

Gaves W., Barbera T., Braun J.B., Imas L. 2008. Measurements and Simulation of Pressure Distribution on Full Size Scales, *in the proceeding of The 3rd High Performance Yacht Design Conference (HPYDC3)*, Dec. 2nd-4th, Auckland, New Zealand.

Horton, H. P., 1968. Laminar Separation in Two and Three-dimensional Incompressible Flow. *PhD Dissertation, University of London*.

Puddu P., Erriu N., Nurzia F., Pistidda A., Mura A., 2006. Full Scale Investigation of One-Design Class Catamaran Sails, *in the proceeding of The 2nd High Performance Yacht Design Conference (HPYDC2),* Febr. 14th-16th, Auckland, New Zealand.

Viola, I.M., Flay, R.G.J., 2010. Full-scale Pressure Measurements on a Sparkman & Stephens 24-foot Sailing Yacht, *J. Wind Eng. Ind. Aerodyn*., 98, 800–807.
*d*oi:10.1016/j.jweia.2010.07.004

Warner, E.P., Ober, S., 1925. The Aerodynamics of Yacht Sails. *Proc. 3rd General Meeting of the Society of Naval Arch. and Marine Eng.*, Nov. 12th -13th, New York.

Wilkinson, S., 1984. Partially Separated Flows Around 2D Masts and Sails, *PhD Dissertation, University of Southampton.*

Figures

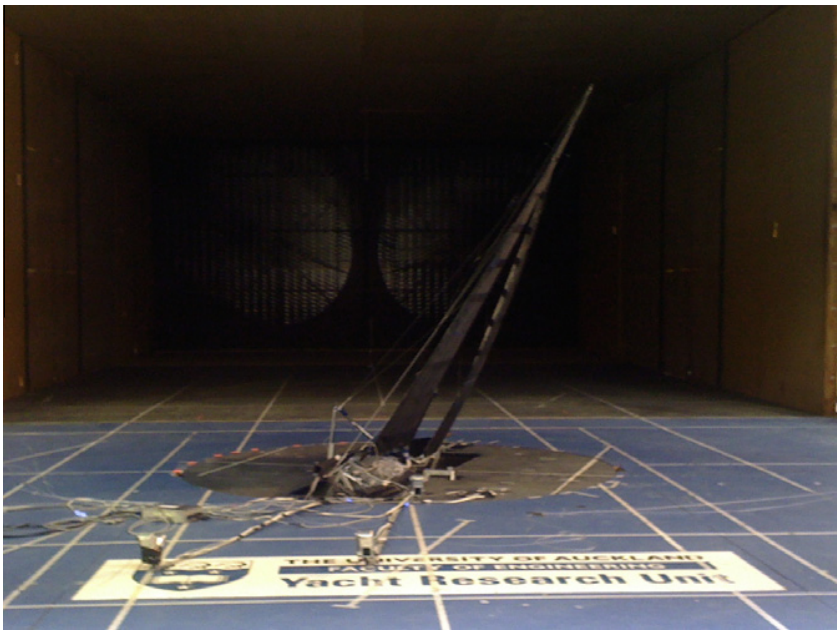

Figure 1: Wind velocity triangle for a yacht sailing upwind.

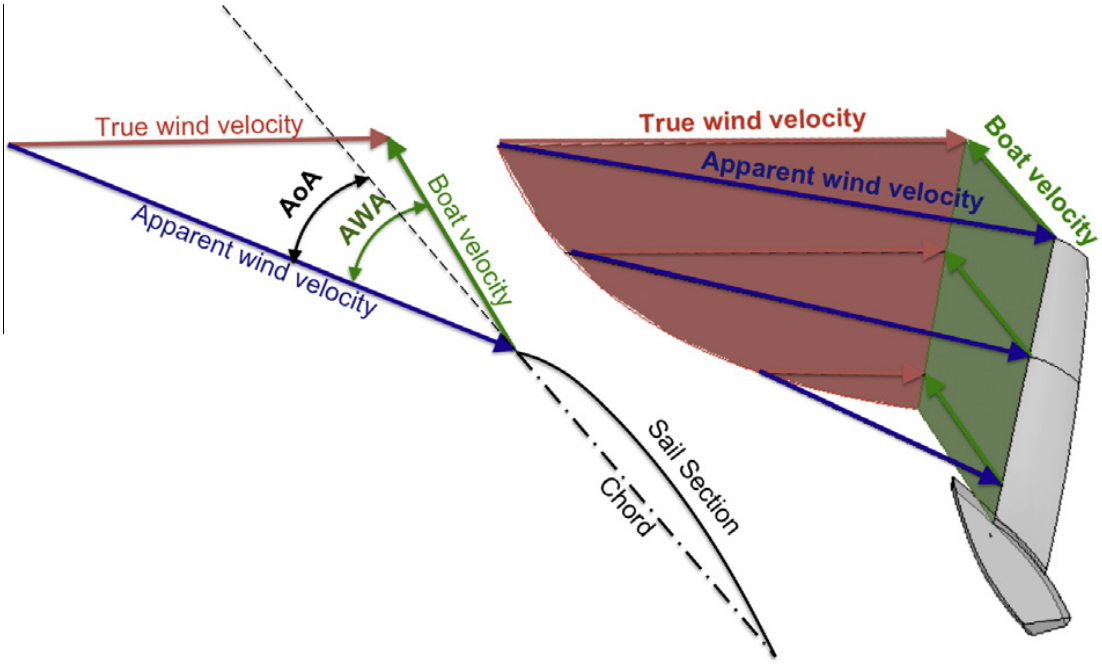

Figure 2: A photograph of the wind tunnel test setup at the Yacht Research Unit, looking upstream.

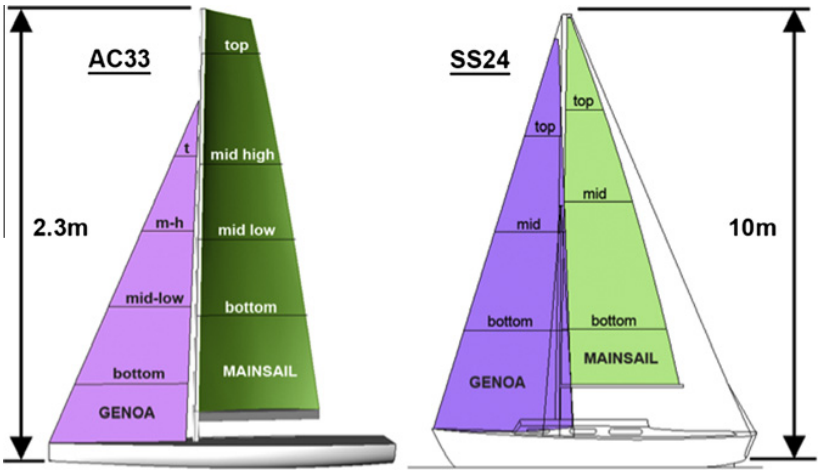

Figure 3: Layout of the model AC33 and the SS24 sailplans.

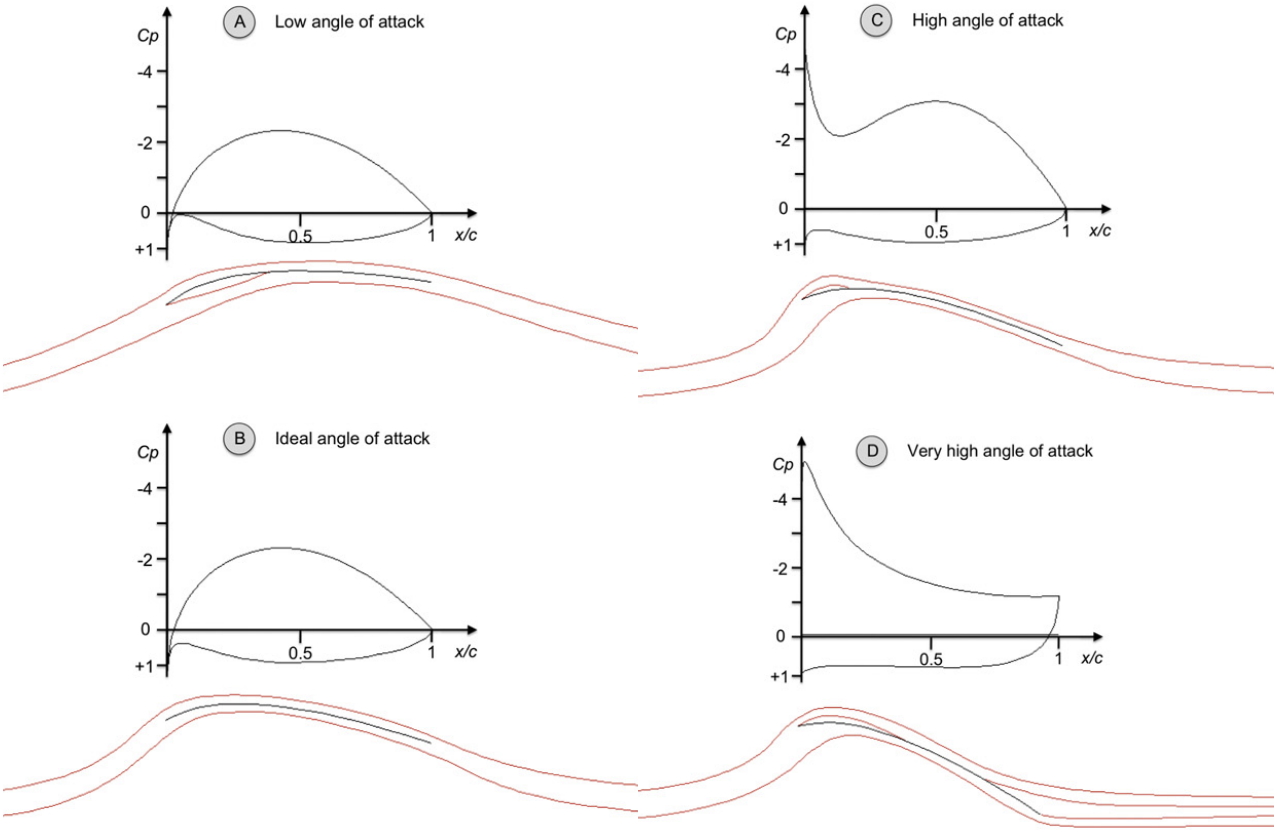

Figure 4: Schematic diagram of the expected flow fields around a headsail chord at 5 angles of attack, and the corresponding *Cps*.

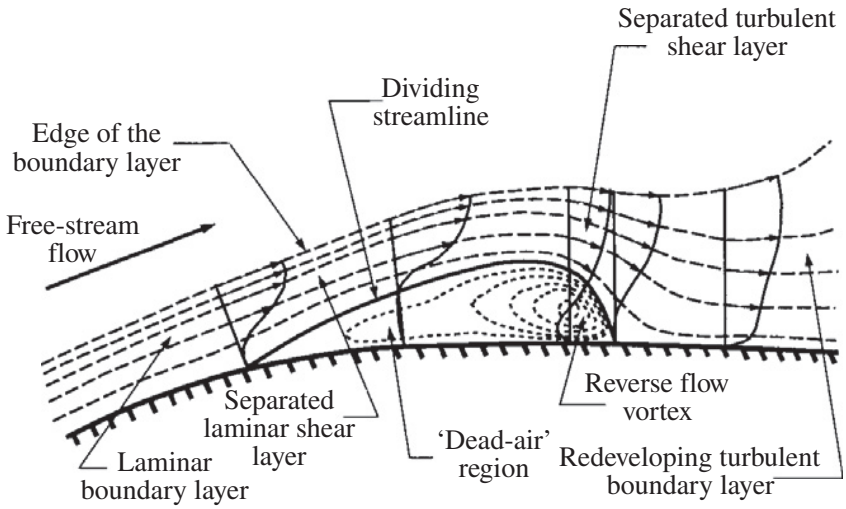

Figure 5: Schematic diagram of the short LE bubble type (Alam and Sandham, 2000).

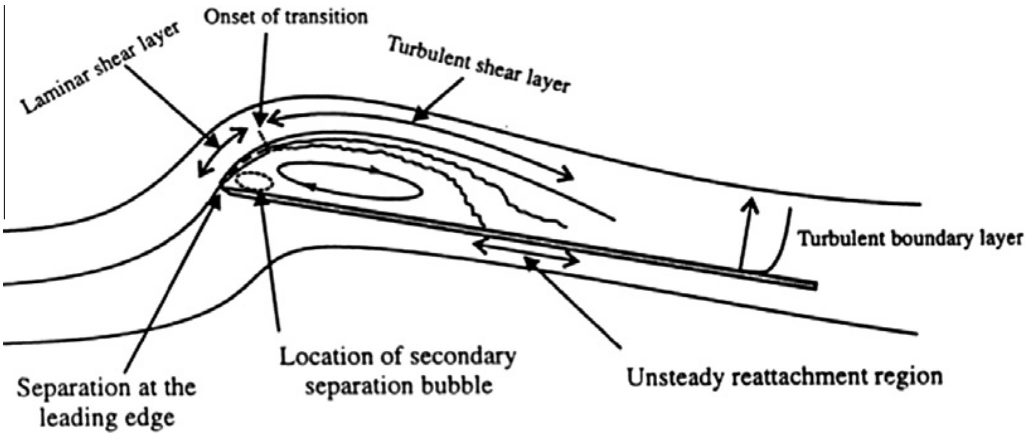

Figure 6: Schematic diagram of the long LE bubble type (Crompton and Barret, 2000).

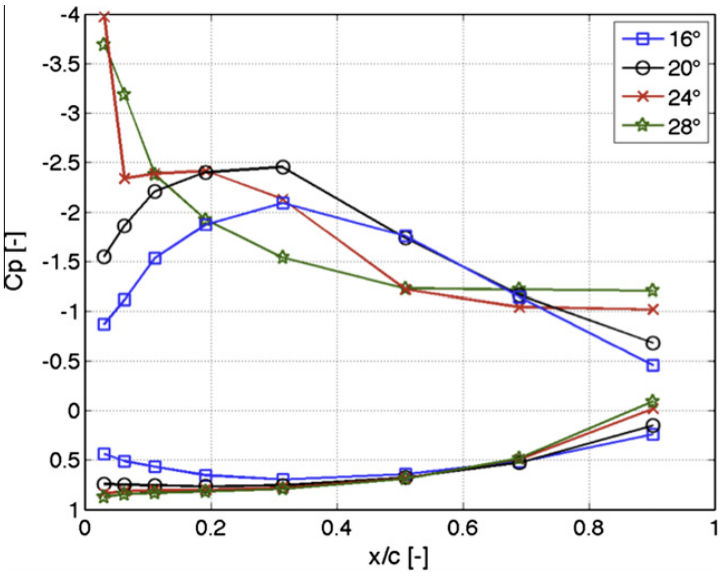

Figure 7: Leeward and Windward *Cp*s on the model-scale headsail.

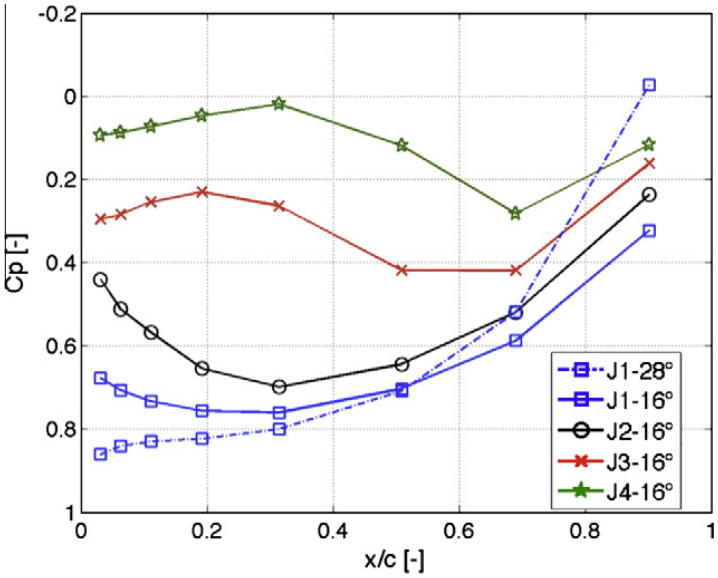

Figure 8: Windward *Cp* on the model-scale headsail.

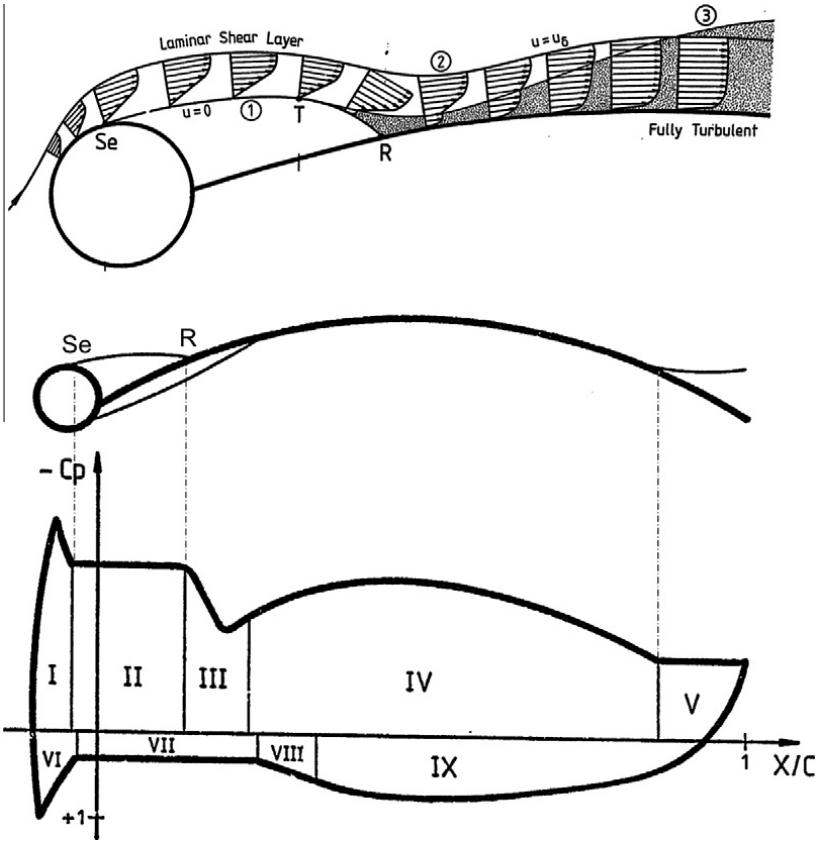

Figure 9: Schematic diagram of the flow field and the related *Cps* around a mast/mainsail (Wilkinson, 1984).

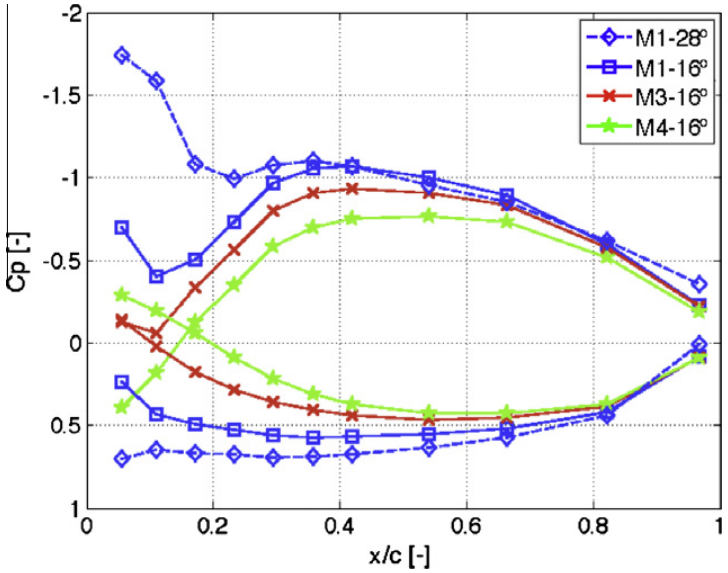

Figure 10: Leeward and Windward *Cp*s measured on the model-scale mainsail.

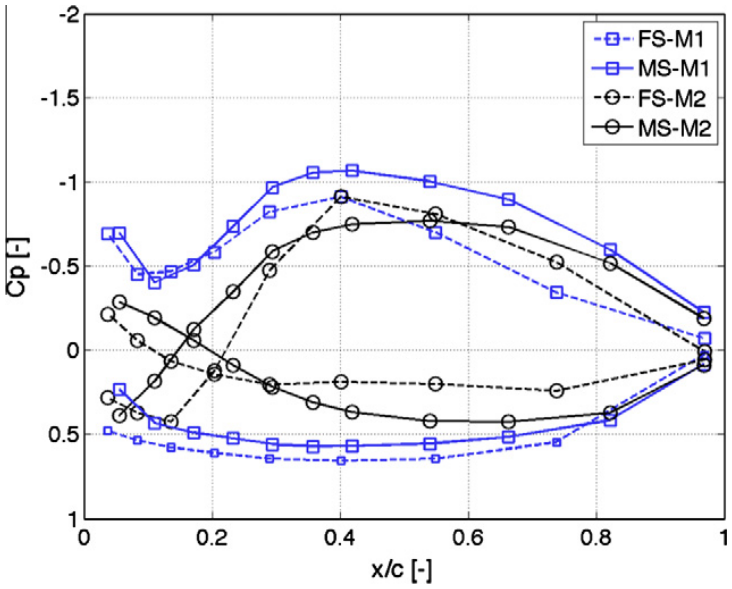

Figure 11: Leeward and windward *Cps* on the model-scale and full-scale mainsails.